International Journal of Mechanical Sciences 286 (2025) 109862



Contents lists available at ScienceDirect

International Journal of Mechanical Sciences

journal homepage: www.elsevier.com/locate/ijmecsci





A flexi-limbed electroactive frame for gripping and locomotion: Structural optimization

Wenjie Sun [a,b], Yuejun Xu [a], Majid Taghavi [a,*]

[a] Department of Bioengineering, Imperial College London, London, United Kingdom
[b] School of Mechanical and Precision Instrument Engineering, Xi'an University of Technology, Xi'an, China

ARTICLE INFO

Keywords:
Electrostatic actuator
Soft robotic
Electromechanical model
Dielectrophoretic liquid zipping
Electro ribbon

ABSTRACTS

Electrostatic soft actuators are widely employed in soft machines due to their fast response, low energy consumption and noise, high energy density, and ease of control. This paper presents an electrostatic flexi-limbed actuation building block based on the dielectrophoretic liquid zipping concept. We establish a model to describe its performance using the theory of large deformation of beams and the energy analysis method. The effectiveness and accuracy of the proposed mathematical model were validated through experiments. Using this model, we investigated the influence of various design parameters on the actuator's static actuation performance. Additionally, we experimentally analyzed the actuator's output force under static voltage and its dynamic behavior under alternating excitation. Furthermore, we evaluated the actuator's locomotion performance in a soft inchworm-like robot by integrating it with a unidirectional wheel assembly. This research provides exploratory experience and new ideas for the design and application of further electro-ribbon actuators.

1. Introduction

Soft robots developed from compliant materials like silicone rubber and hydrogel offer the unique advantage of softness, environmental adaptability, multifunctional interaction, embodied intelligence and potential biocompatibility. They have a high potential to address the limitation of traditional rigid robots, making them a focal point in current developments in robotics research [1–3]. As their core components, multiple soft actuation technologies have been introduced, actuated through diverse stimulation such as electric [4–6], magnetic [7–9], thermal [10–12], optical [13–15], pneumatic [16–18], and chemical reactions [19–21]. Among these, electrostatic actuators stand out for their controllable operation, fast response, low energy consumption and minimal noise. They leverages the maxwell stress generated by the attractive force between opposite charges to induce actuation deformation [22–24]. This phenomena has been widely investigated in dielectric elastomers, which applies this maxwell stress across the elastomer's surface [25–27] and found wide-ranging applications in biomimetic fish [28–30], aerial reconnaissance micro-vehicles [31–33], crawling robots [34–36], adjustable optical devices [37–39], generators [40–42], and cellular engineering [43,44]. However, their potential is limited with the high failure risk of electrical breakdown in dielectric elastomers, the need for pre-stretching, and the inherent viscoelasticity of the material [45–48].

The hydraulic amplified electrostatic actuator replaces the solid dielectric with a pouch containing liquid dielectric. This not only enables the actuation process to have self-healing capability during electric breakdown through the liquid, but also enhances actuation performance compared to the dielectric elastomer under the same voltage thanks to the hydraulic amplification of the liquid dielectric [5,49]. The Peano-HASEL simplifies the preparation process [50–52] and improves the energy density of the actuator, while expanding the design options of the actuator due to the use of a flexible inextensible encapsulation layer [53–55]. However, owing to the limitation of the flexible wrapping layer, the maximum theoretical deformation of Peano-HASEL is 24%. With a strain-amplified pulley system, it can achieve a maximum strain of 50% [56]. Meanwhile, the liquid dielectric in the pouch increases the weight and complexity of the fabrication.

The Electro-ribbon actuator (ERA), uses electrostatic zipping force generated between two insulated flexible electrodes to achieve high contraction deformation of 99.8% while matching the specific energy and power of skeletal muscle [57]. In EBA, a tiny bead of liquid dielectric (silicone oil) is sufficient to amplify the electrostatic force, theoretically up to 120 folds. This applies to the effective zipping point

* Corresponding author.
E-mail address: m.taghavi@imperial.ac.uk (M. Taghavi).

https://doi.org/10.1016/j.ijmecsci.2024.109862
Received 20 May 2024; Received in revised form 26 September 2024; Accepted 27 November 2024
Available online 28 November 2024
0020-7403/© 2024 The Authors. Published by Elsevier Ltd. This is an open access article under the CC BY license (http://creativecommons.org/licenses/by/4.0/).

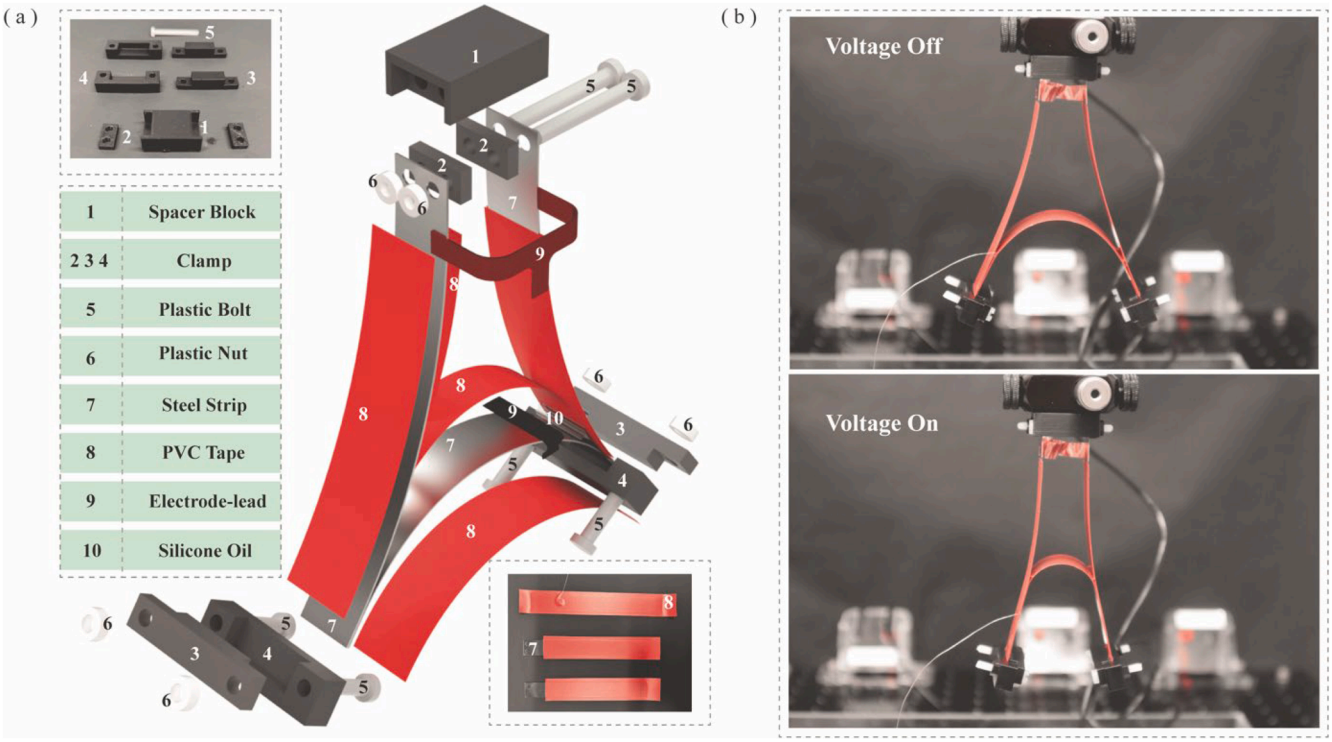


Fig. 1. Structural design and actuation deformation of the flexi-limb actuator: (a) exploded view of the actuator and its component information. Both the fixing and clamping components are fabricated using 3D printing; (b) snapshots of the actuation before and after the application of voltage.

through dielectrophoretic force with no hydraulic force transmission. This enables lightweight design with reduced complexity of the structures for optimizing the materials, loading, stability and control. While this electrophoretic zipping actuation concept has been widely exploited for micro aerial vehicles [58], micropump drives [59], bionic fingers [60], multidirectional motion [61], and muscle-mimetic actuators [62], theoretical modeling has mainly focused on the fundamental bow-shaped EBA structures [63,64]. Its application in grippers and mobile soft robots has yet to be investigated.

In this paper, we introduce a novel Flexi-Limb ribbon structure, which can be used as a building block actuation in manipulation and soft mobile robots, actuated by the dielectrophoretic liquid zipping concept that requires only a small amount of silicone oil to significantly amplify the electrostatic force by enhancing the dielectric breakdown strength and the dielectric constant of the medium. We establish a mechanistic analysis model to describe the performance of the actuator, by combining the large deformation theory of beams with an energy analysis method. We experimentally validate and analyze its effectiveness and accuracy. We then investigate the impact of various design parameters on the actuator's performance based on the theoretical model. Additionally, we assess the actuation behavior of the flexi-limbed actuator under dynamic excitation through the experimental analysis. Finally, a soft inchworm-like robot that can move in a single direction by combining the actuator with the specially designed unidirectional wheels is demonstrated. This paper not only advances the design theory and analysis method of an EBA functional actuation block, but also provides insights for applying EBA in crawling soft robots.

The remainder of the paper is organized as follows: In Section 2, the structural design and theoretical modeling of the flexi-limbed actuator are analyzed. Section 3 explores the steady-state actuation performance and its effective parameters. Section 4 discusses the force measurement and dynamic response of the flexi-limbed actuator. Finally, Section 5 presents a summary of the main findings.

2. Structural design and theoretical modeling of flexi-limbed actuator

This section provides an investigation of the actuator's structural features and fabrication process. Furthermore, a mathematical model is developed to characterize the electro-mechanical coupling behavior of the actuator, based on an analysis of the stress distribution in the flexible electrodes.

Fig. 1 (a) shows the 3D schematic of the Flexi-Limb actuation design. The actuator structure consists of three carbon steel strips (1.1274 carbon steel, h+s Prazisionsfolien Gmbh, Germany), insulating PVC tapes (AT7 PVC Electrical Insulation Tape, Advance Tapes, UK), a spacer block, 3D printed clamp, plastic bolts, and lead wires. Each electrode measures 12.7 mm in width, covered by PVC tape on both sides. The thickness of the lateral and bottom electrodes is 0.15 mm, and 0.07 mm, respectively. Plastic bolts secure the two lateral electrodes to the spacer block at one end, while clamps connect them to the bottom electrode at the other end. Silicon oil (50 cSt, Sigma-Aldrich, USA) is applied at the lateral-bottom electrode junction, acting as a liquid dielectric in the electrostatic zipping point. When voltage is applied between the lateral and bottom electrodes, they zip together, leading to the entire actuator to reach a new equilibrium configuration, as shown in Fig. 1 (b).

Analyzing the actuation behavior of the flexi-limb, consisting of three flexible linked ribbons, and driven by a non-linear electrostatic force, requires a comprehensive electrotechnical model. We employ the large deformation analysis of Euler–Bernoulli beams, coupled with the energy analysis, to investigate the actuation behavior of the Flexi-Limb under different excitations and assess the key parameters affecting its performance.

Fig. 2 (a) shows the actuator diagram in both relaxed and actuated states. In the relaxed state, two lateral electrodes, each of length L_0, are connected at one end to a spacer block of width D_0 and fixed at the other end to a bottom electrode of length C_0 . The lateral and bottom electrodes have a width of W and thicknesses of T_L and T_B, respectively. Both sides of the electrodes are covered by PVC tape with a thickness of t_p. In

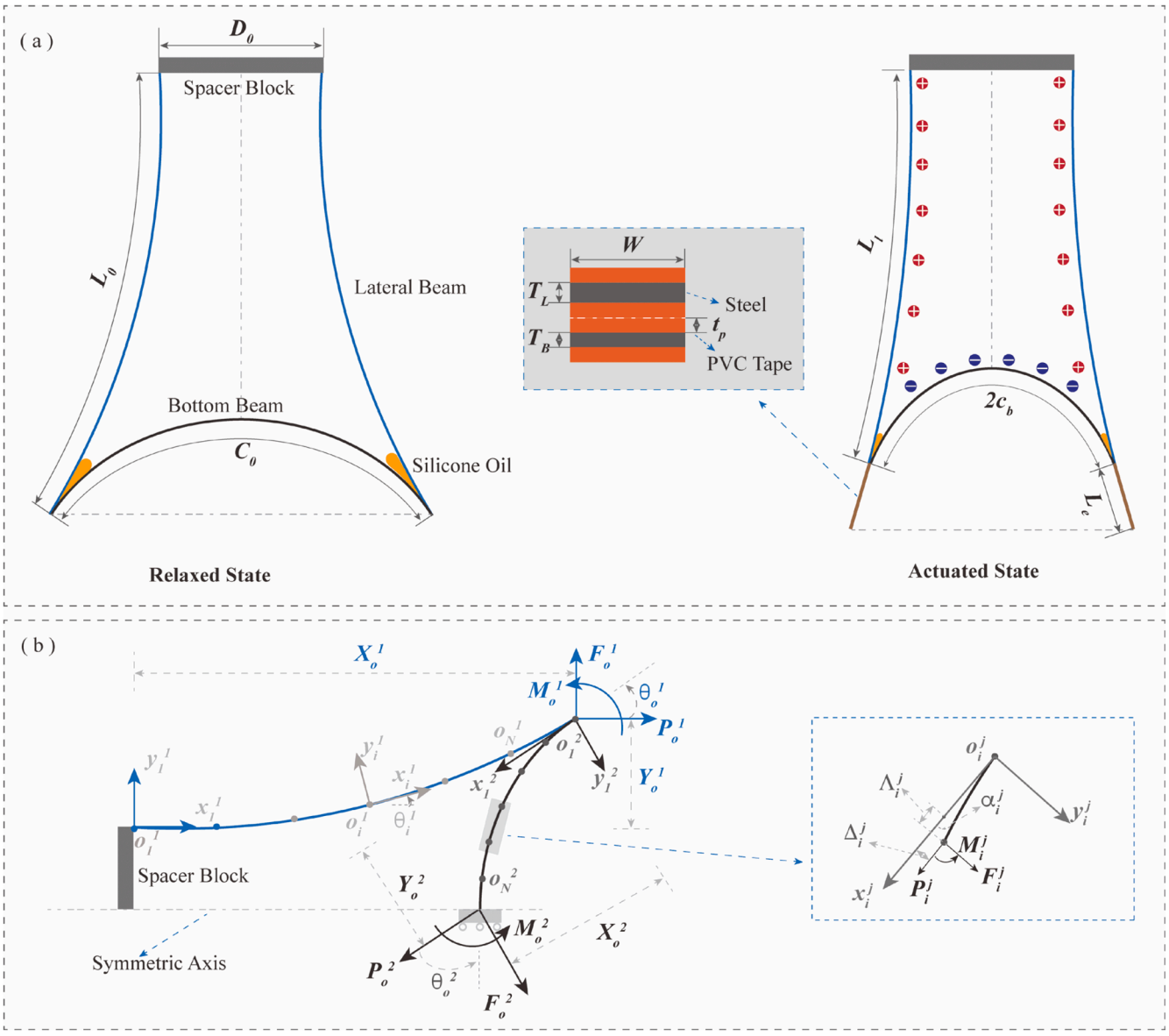


Fig. 2. A simplified model of the Flexi-Limb actuator with force analysis: (a) geometric configuration of the actuator in the relaxed and actuated states; (b) force analysis of the lateral and bottom electrodes in one half of the actuator during actuation. The subfigure illustrates the force conditions of the micro-beam unit.

the actuated state, the lateral and bottom electrodes zip together under electrostatic force, defining a zipping length as L_e. In this case, the active bend lengths of the lateral and the bottom electrodes vary to L_l and $2c_b$, respectively. Considering the symmetry of the actuator, force analysis is conducted on one side of the structure (as shown in Fig. 2 (b)). Analyzing the minimum value of the energy of the system is an effective method for determining the equilibrium state of the actuator under external excitation, a widely used approach in modeling and analyzing electrically-driven actuators [65–67]. Neglecting energy dissipation of the system during actuation, the total energy of the system $U_t = V^l + V^b + E_e - E_b$, where V^l and V^b represent the bending strain energy, stored in the lateral and bottom electrodes, respectively. E_e is the stored electrostatic energy, which is dominated in the zipping region, and E_b represents the electrical energy source.

When the actuator is excited by a voltage Φ, the lateral electrodes zip with the bottom electrodes, with each side experiencing a zipping length L_e. The electrostatic energy E_e stored in the zipped region can be written as a function of the total capacitance of the zipped area and the excitation voltage applied to the actuator as $C\Phi^2/2$, which can be expressed as:

$$E_e = \frac{1}{2}\frac{\varepsilon_0 \varepsilon_r L_e W}{2t_p}\Phi^2, \tag{1}$$

Here ε_r and t_p represent the relative dielectric constant and thickness of the PVC tape covering the lateral and bottom electrodes respectively, and W denotes the width of the electrode.

The electric energy E_b provided by the power source is the energy source for this actuation. We assume there is no gap for silicone oil between the two electrodes that have already been zipped together by the electrostatic force. Considering the constant voltage of the power source Φ, charge Q flows from it to the actuator, thus the provided energy can be expressed as ΦQ. This can be rewritten as below once Q is replaced by $C\Phi$:

$$E_b = \frac{\varepsilon_0 \varepsilon_r L_e W}{2t_p}\Phi^2 . \tag{2}$$

To provide an accurate description of the deformation features of the lateral and bottom electrodes during the actuation and to determine the strain energies V^l and V^b, we consider the lateral and bottom electrodes

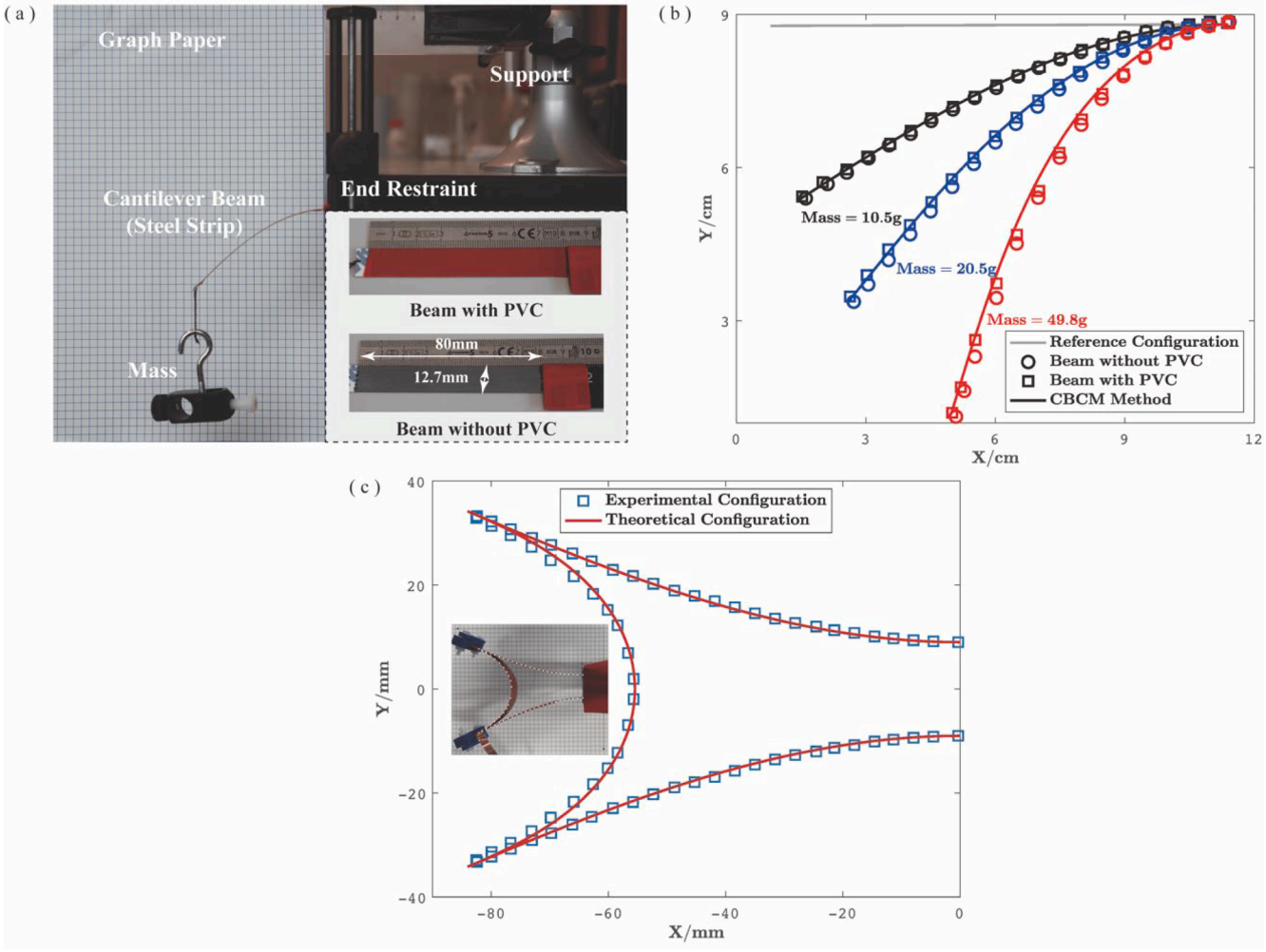


Fig. 3. Passive mechanical analysis: (a) bending deformation experiments of the electrode beam, and its geometric dimensions; (b) comparison between experimental and theoretical results of cantilever beam deformation under different loads; (c) comparison of actual deformation in a relaxed state with theoretical simulations. The subfigure illustrates the marked points on the lateral and bottom beams of the actuator during the experiment.

as Euler–Bernoulli beams with large deformations. For simplicity, we refer to the lateral electrodes as lateral beams and the bottom electrodes as bottom beams. The Chained Beam Constraint Model (CBCM) method is widely employed for modelling the large deformation analysis of beams, due to its high adaptability, solution accuracy, and computational speed, especially in bistable structures and flexible mechanisms. This method divides the large deformation beam into several micro-beam units using the discrete concept, establishes equilibrium equations for each segment of micro-beam based on the classical beam theory, and ultimately obtains the equilibrium equations for the entire beam structure by combining the force relationship between adjacent micro-beams. It, therefore, can effectively solve the large deformed bending problems of straight beams, curved beams, and beams with variable lengths [68–70].

Fig. 2 (b) illustrates the force diagrams of the lateral and bottom beams and their reference coordinate systems while using the CBCM method. The origin of the reference coordinate system o_1^l for the lateral beam is set at the connection between the lateral beam and the spacer block. The loads on the lateral beam at the end include P_o^1, F_o^1, and M_o^1 (with the directions shown in Fig. 2 (b)), while the displacements and angles of rotation of the lateral beam at the end in the reference coordinate system $x_1^l o_1^l y_1^l$ are denoted as X_o^1, Y_o^1, and θ_o^1, respectively. The reference coordinate system o_1^2 for the bottom beam is set at the junction of the bottom and lateral beams, with the x_1^2 axis aligned along the tangent direction of the lateral and bottom beams. The loads on the bottom beam at the end consist of P_o^2, F_o^2, and M_o^2 (as shown in the Fig. 2 (b)), and the displacements and angles of rotation are X_o^2, Y_o^2, and θ_o^2, respectively.

Appendix A presents the detailed expression for the bending strain energy of beam using the CBCM method. Consequently, the total energy U_t of the entire system can be expressed as:

$$U_t = V^l + V^b + E_e + E_b = \sum_{i=1}^{N} \left\{ \frac{NE_lI_l}{L_l} \left[\frac{(t_l p_i^l)^2}{24} + \begin{bmatrix} \delta_i^l & \alpha_i^l \end{bmatrix} \begin{bmatrix} 6 & -3 \\ -3 & 2 \end{bmatrix} \begin{bmatrix} \delta_i^l \\ \alpha_i^l \end{bmatrix} - \frac{(p_i^l)^2}{12600} \begin{bmatrix} \delta_i^l & \alpha_i^l \end{bmatrix} \begin{bmatrix} -9 & 4.5 \\ 4.5 & -11 \end{bmatrix} \begin{bmatrix} \delta_i^l \\ \alpha_i^l \end{bmatrix} \right] \right.$$
$$\left. + \frac{NE_bI_b}{c_b} \left[\frac{(t_b p_i^b)^2}{24} + \begin{bmatrix} \delta_i^b & \alpha_i^b \end{bmatrix} \begin{bmatrix} 6 & -3 \\ -3 & 2 \end{bmatrix} \begin{bmatrix} \delta_i^b \\ \alpha_i^b \end{bmatrix} - \frac{(p_i^b)^2}{12600} \begin{bmatrix} \delta_i^b & \alpha_i^b \end{bmatrix} \begin{bmatrix} -9 & 4.5 \\ 4.5 & -11 \end{bmatrix} \begin{bmatrix} \delta_i^b \\ \alpha_i^b \end{bmatrix} \right] \right\} - \frac{1}{2} \frac{\varepsilon_0 \varepsilon_r L_e W}{2t_p} \Phi^2, \tag{3}$$

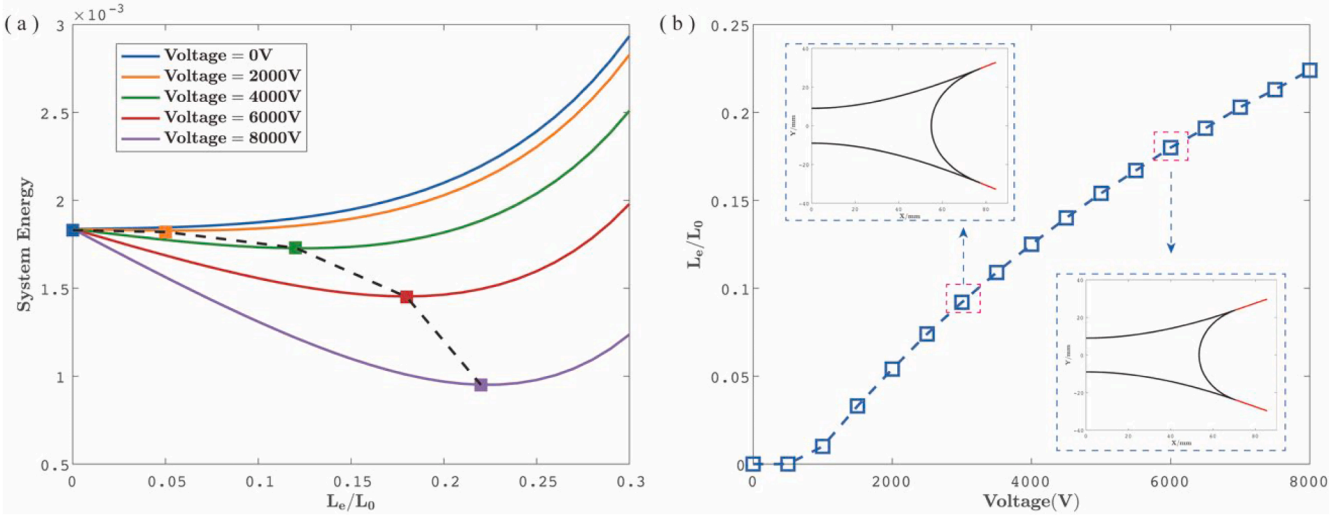


Fig. 4. The variations of the system energy of the actuator with the excitation voltage: (a) system energy curve of the actuator under different excitation voltages; (b) zipping ratio of the actuator in equilibrium under different excitation voltages. The two subfigures show the configurations of the actuator at 3 kV and 6 kV, with the red areas indicating the zipping regions of the lateral and bottom beams.

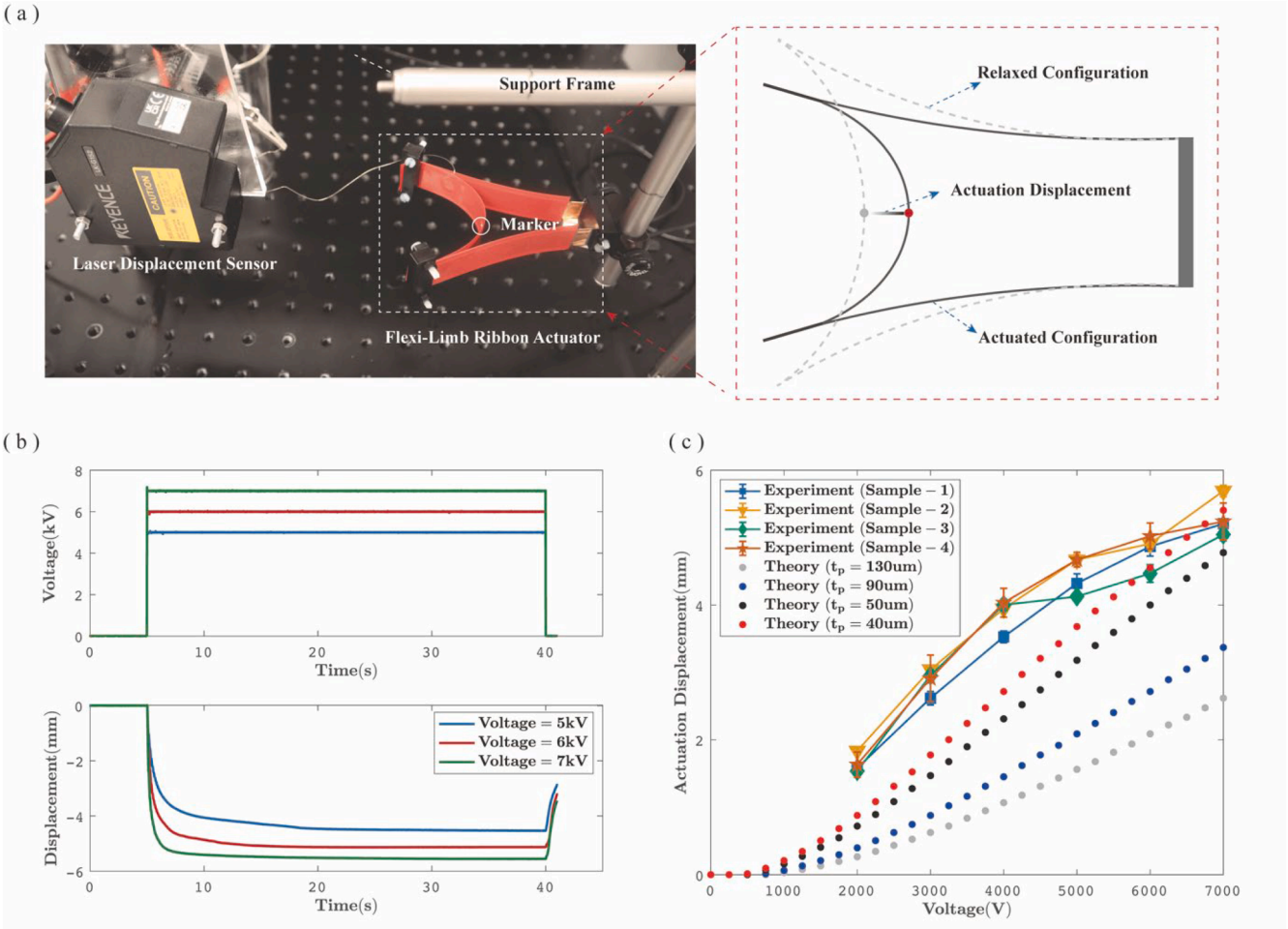


Fig. 5. Experimental setup for performance testing of the Flexi-Limb actuator and the actuation behaviors: (a) experimental platform for actuator displacement measurement and schematic diagram of performance testing principles; (b) typical displacement curves of the actuator under the three actuation voltages; (c) displacement curves versus voltage for four samples compared to the theoretical model. In the theoretical model, four PVC film thicknesses were selected: 40 μm, 50 μm, 90 μm, and 130 μm.

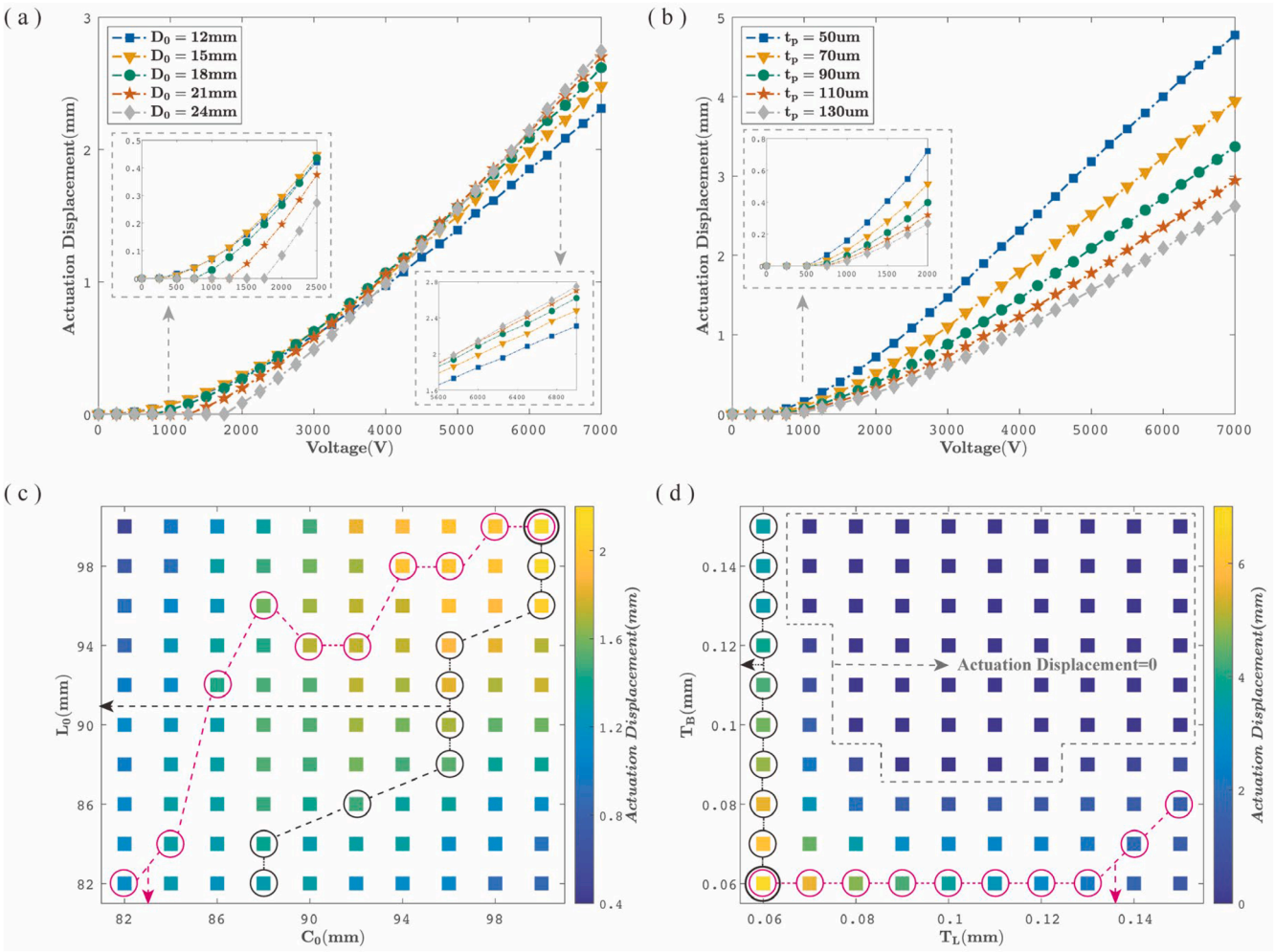


Fig. 6. Effects of different design parameters on the performance of the Flexi-Limb actuator including: (a) the spacer block width (D_0) at $t_p = 130um$. The subfigure illustrates the variation of actuation displacement across different parameter regions; (b) PVC insulating tape thickness at $D_0 = 18mm$; (c) the lateral and bottom electrodes lengths at 5 kV; and (d) the lateral and bottom electrodes thicknesses at 5 kV.

Here L_l and c_b denote the effective lengths of the lateral and bottom electrodes in Fig. 2 (b), respectively, where $L_l = L_0 - L_e$ and $c_b = C_0/2 - L_e$. By combining Eqs. A2, A3, and A4, the total energy of the system can be represented as a function of the excitation voltage Φ and the zipping length L_e. Using the energy analysis method, the zipping length L_e of the actuator under the excitation voltage can be determined by identifying the point where the energy of the system is minimal. Therefore, the actual configuration of the actuator in the reference coordinate system $x_1^1 o_1^1 y_1^1$ and the displacement XX_o^2 are determined as:

$$XX_o^2 = -X_o^2 cos\theta_o^1 + Y_o^2 sin\theta_o^1 + X_o^1 \tag{4}$$

It implies that the actuation displacement Act_{-dis} (actuation displacement) of the actuator under the excitation of voltage Φ is:

$$Act_{-dis} = XX_o^2(\Phi = 0) - XX_o^2(\Phi > 0)\ . \tag{5}$$

3. Steady-state actuation performance and its effective parameters

In this section, the reliability and accuracy of the Chained Beam Constraint Model (CBCM) method for analyzing large beam deformations are validated through experimental testing. Next, the electro-mechanical coupling model developed in Section 2 is experimentally verified and discussed. Finally, based on this model, the effects of various design parameters on the actuator's performance are investigated.

When designing for the dielectrophoretic liquid zipping actuator, it is crucial to ensure that the lateral and/or bottom electrodes are shielded by an insulator (such as PVC electrical tape) at the interface. Covering both sides of each electrode enhances bonding strength and symmetry. Therefore, we first investigate the impact of the PVC-covered layer on the beam bending deformation. We investigate the behavior of cantilever beams, made from steel strips with or without PVC, under varying loads using experimental and CBCM methods. The electrode beams had a length of 80 mm, width of 12.7 mm and thickness of 0.15 mm, as shown in Fig. 3 (a)-(b). Results show that under equivalent loading, PVC-covered beams exhibit marginally smaller and negligible deformation compared to those without PVC. Simulation of the cantilever beam configurations under different loads suggests that the CBCM offers an accurate approach for simulating large deformations, assuming a modulus of elasticity of 170 GPa for the electrode beams. Since there is no zipping of the actuator in the relaxed state, its configuration can be directly simulated using Equations A.1-A.4 (Fig. 3 (c)), which aligns well with the actual observations.

Analyzing how the systems' energy varies with the excitation voltage is crucial for determining the equilibrium state of the actuator. Fig. 4 (a) shows the relationship between the system energy U_t and the zipping ratio (L_e/L_0) at different excitation voltages Φ. It can be seen that, regardless of the excitation voltage Φ, there is a point of minimum value in the system energy curve. The horizontal axis corresponding to the

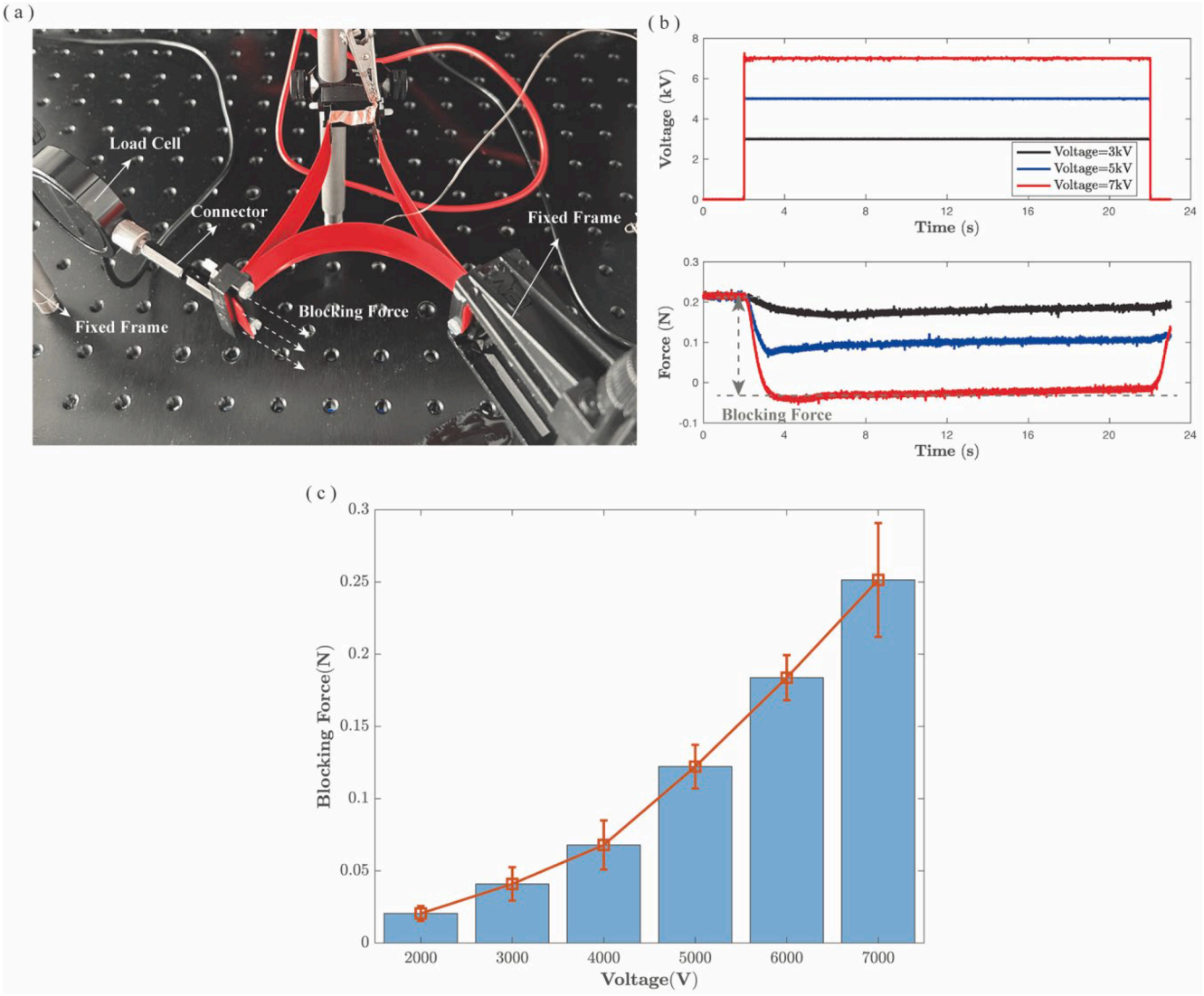


Fig. 7. Force response of the Flexi-Limb actuator: (a) blocking force testing experimental platform for the actuator; (b) typical force curves under three actuation voltages; (c) blocking force and voltage curves of the actuator across a drive voltage range of 2 kV to 7 kV.

minimum value represents the ratio of the electrode zipping distance L_e to the lateral electrode length L_0 at this equilibrium state. Higher excitation voltage Φ results in a larger zipping ratio, indicating a greater displacement in this configuration. This effect arises from increased electrostatic forces between the lateral and bottom electrodes, as shown in Fig. 4 (b).

Fig. 5 (a) shows the experimental setup for testing the actuator's performance. To remove the effect of gravity, the actuator is fixed horizontally on the support frame. A laser displacement sensor (LG-GD500, Keyence, Japan) tracks the displacement change of the marked point at the bottom electrode of the actuator, while voltage application and displacement data acquisition are handled by a computer and a data acquisition device. The actuator's leads were connected to opposite polarity of the power supply, with the specific voltage curves shown in the top subplot of Fig. 5 (b). In the experiment, the lengths of the lateral and bottom electrodes of the actuator, L_0 and C_0, are 88.5 mm and 94.5 mm, respectively. The electrode thicknesses T_L and T_B measures 0.15 mm and 0.07 mm, respectively while the electrode widths W is 12.7 mm and the spacer block width D_0 is 18 mm. Four identical actuator samples are tested under the same voltage excitation, generating three sets of data each. Fig. 5 (c) presents the actuation displacement at different voltages. Our proposed theoretical model describes the actuation behavior under different excitation voltages, revealing an approximately twofold discrepancy compared to the experimental results. We attribute this disparity to the simplifications made in calculating the electrostatic energy. Initially, the system was modelled as an ideal capacitance with a single layer of PVC insulation, assuming a relative permittivity of 4.62 and a thickness of 130 um [57]. However, the electric tape used as the insulator in the experiments is a composite material, consisting of PVC and an additional adhesive silicone layer. One major factor we overlooked is the effect of interfacial polarization and charge accumulation, which can greatly amplify electrostatic forces—especially when different plasticizers are used in the PVC formulation [71]. Additionally, the compressibility of the tape allows its thickness to change under electrostatic pressure [63]. Fig 5 c shows how altering the thickness of the PVC tape affects the anticipated displacements in our model. Although the proposed actuator is a complex electromechanical coupling system, the primary source of deformation lies in the significant deflections of the side and bottom beams. To analyze these large deformations, the Chained Beam Constraint Model (CBCM) method is employed, a highly accurate approach widely used for beam deformation analysis. Furthermore, the theoretical model developed in this paper is a static model, which only examines the actuator's configuration deformation before and after voltage application,

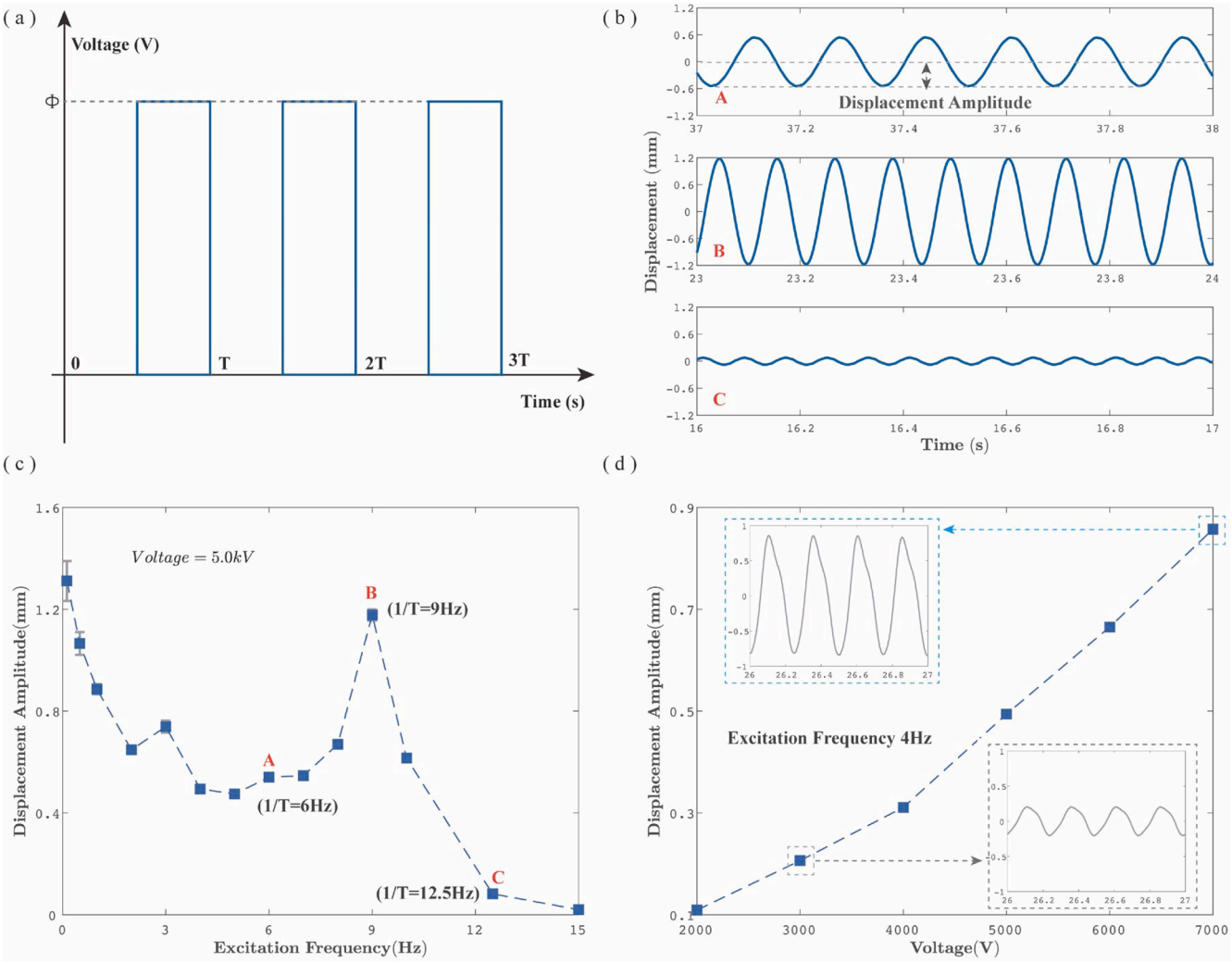


Fig. 8. Dynamic actuation performance of the Flexi-Limb actuator: (a) voltage signal applied to the actuator; (b) actuator displacement at 5 kV under three different excitation frequencies (6 Hz, 9 Hz, 12.5 Hz); (c) actuator displacement at 5 kV across a frequency range of 0.125 Hz to 15 Hz; and (d) actuator displacement at an excitation frequency of 4 Hz, with a drive voltage amplitude ranging from 2 kV to 7 kV.

without considering the actuation process itself or the influence of silicone oil flow. This static model is, therefore, well-suited to capturing the electromechanical coupling behavior of the actuator. To mitigate experimental error, four actuators were fabricated using identical design parameters, and multiple sets of measurements were conducted.

The design parameters of the actuator have a significant impact on determining its actuation performance, as highlighted in Fig. 6. The spacer block width D_0 shows varying effects on actuation performance across different excitation voltages. For low excitation voltages, a narrower spacer block width D_0 results in larger actuation displacement, whereas under high excitation voltage, a wider spacer block width D_0 leads to increased actuation displacement. Furthermore, a larger spacer block width D_0 corresponds to the higher critical voltage required to initiate actuator deformation, as shown in Fig. 6 (a). Consistently, under different excitation voltages, the thickness of the PVC insulating tape influences actuation performance. A thinner insulator results in larger actuation displacement under the same voltage due to the higher electrostatic force generated under the same voltage, as shown in Fig. 6 (b).

Figs. 6 (c) and (d) show the influence of lateral and bottom electrode length and thickness on actuator performance under an excitation voltage $\Phi = 5kV$, respectively. The red circle in Fig. 6 (c) represents the optimal length of the lateral electrode that generates the maximum actuation displacement under the constant length of the bottom electrode, whereas the black circle shows the optimal length of the bottom electrode that generates the maximum actuation displacement under the constant length of the lateral electrode. In general, the larger the lateral electrode and the bottom electrode are, the larger the actuation displacement of the actuator is at the same excitation voltage. Fig. 6 (d) shows that when the thicknesses of lateral and bottom electrodes are not carefully matched, the actuator cannot generate displacement under an excitation voltage $\Phi = 5kV$, as shown by the grey dotted line in the figure. Similar to electrode length, optimal combinations of the lateral and bottom electrode thicknesses exist to maximize actuation displacement, as shown by the red and black circles in Fig. 6 (d).

The aforementioned studies demonstrate that an increase in the spacer block width (D_o) or the PVC film thickness (t_p) leads to a higher critical voltage required to initiate actuator deformation. However, as the PVC film thickness t_p increases, the actuation displacement decreases under the same voltage. The impact of spacer block thickness D_o, on actuation displacement varies with the applied voltage. At lower voltages, a larger D_o results in reduced actuation displacement, whereas at higher voltages, the displacement increases as D_o becomes larger. At a constant excitation voltage, there is an optimal correlation between the lateral electrode length (L_o) and the bottom electrode length (C_o), indicating that for a given L_o, an ideal C_o can be determined, and vice versa.

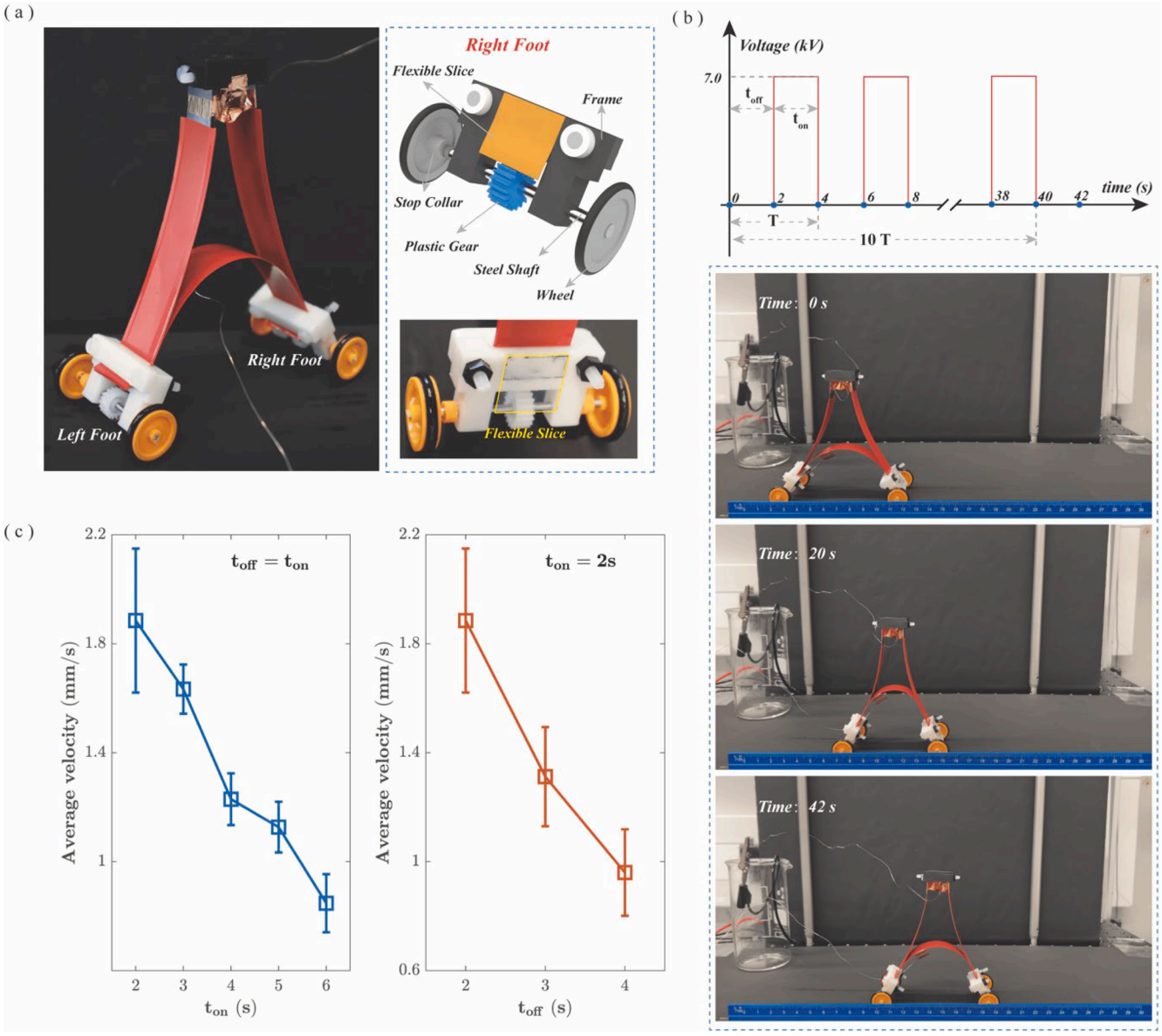


Fig. 9. Inchworm-like robot designed with the flexi-limbed actuator: (a) photograph of the soft robot and its foot structure, demonstrating unidirectional motion achieved through the engagement of flexible paddles with plastic gears; (b) snapshots of the soft robot running across 10 loading cycles, with a voltage amplitude of 7 kV; (c) movement performance of the soft robot under different voltage settings. The left image shows simultaneous variation in both loading and unloading times, while the right image illustrates a constant loading time with varying unloading time.

Additionally, thinner lateral electrode (T_S) and bottom electrode (T_L) result in greater corresponding actuation displacements.

4. Force measurements and dynamic response of the flexi-limbed actuator

This section further explores the actuator's output force characteristics, its dynamic response, and inherent vibration behavior under alternating voltage excitation. Moreover, the actuator's potential for soft robotics applications is demonstrated by integrating it into a unidirectional wheel assembly.

The deformation of the flexi-limb actuator has potential applications in flexible manipulator gripping and robotic locomotion. Therefore, exploring the blocking force of the actuator under static voltage and its dynamic response to alternative voltage is essential for its practical use. Fig. 7 shows the force response of the actuator at different voltages. The upper part of the actuator was secured horizontally to the fixed frame. At the bottom side of the actuator, one end was connected to the fixed load cell (DBCR-10N-002–000, Applied Measurement Ltd., UK) and the other side was anchored to the frame (see Fig. 7 (a)). As seen in the typical signals in Fig. 7 (b), the change in force measured by the load cell under voltage applications denotes the blocking force. These forces at different driving voltages are presented in Fig. 7 (c), revealing that the actuator's blocking force can reach up to 0.25 N at 7 kV . At higher voltages, we observe greater fluctuations in the blocking force. We attribute this to the fact that both the dielectrophoretic and zipping forces become stronger, and therefore, oil and ribbons move faster at higher voltages. This potentially causes dielectric movement and zipping to initiate from one side and leads to an unbalanced force distribution between the two legs until the electrostatic and elastic forces reach equilibrium. This causal effect likely contributes to the increased variability in the measured blocking force during repeated experiments.

The actuator's response to dynamic excitation has been studied using experimental methods, as shown in Fig. 8. Square wave voltage signals,

known for their superior driving energy compared to sinusoidal and triangular waveforms [72,73], are used as input signals, as shown in Fig. 8 (a). Fig. 8 (b) presents the actuation displacement curves at three excitation frequencies (1/T), A (6 Hz), B (9 Hz), and C (12.5 Hz), under 5 kV. The dynamic response amplitude of the actuator is determined as half of the difference between the maximum and minimum displacements, as shown in the top subplot of Fig. 8 (b).

In practical applications, frequencies near the structural resonance frequency are commonly chosen to optimize actuation performance [74–76]. The dynamic response amplitude of the actuator was tested over a frequency range of 0.125 Hz to 15 Hz to identify the resonance frequency. The amplitude of the actuator's displacement response was measured once steady-state vibration was achieved at each excitation frequency. For each frequency, three consecutive tests were conducted to obtain the amplitude-frequency response curves of the actuator across the entire range of excitation frequencies, as presented in Fig. 8 (c). The experimental results reveal a prominent response peak at an excitation frequency of 9 Hz, along with a secondary peak at 3 Hz. Thus, the resonance frequency of the actuator is determined to be 9 Hz. Although the actuator at 0.125 Hz can also achieve the same amplitude as the 9 Hz response displacement, its low driven frequency leads to longer periods and lower response rate. Employing the input signal at the resonance frequency proves to be an effective driving and control strategy. Additionally, at a constant actuated frequency, the amplitude of the dynamic response of the actuator increases with the amplitude of the excitation voltage, since higher excitation voltages induce a stronger electrostatic effect, resulting in more significant deformation of the actuator.

We test the dynamic response of the flexi-limbed actuator in an inchworm-like mobile robot, a bio-inspired concept widely investigated with dielectric elastomers and pneumatic soft robots [77–81]. As shown in Fig. 9 (a), we designed its leg structure based on the principle of the ratchet movement, which enables directional movement of the robot under alternating voltage. In Fig. 9 (b) a snapshot captures the soft robot's motion under dynamic square wave excitation with a voltage of 7kv, a loading period of 4 s and a duty cycle of 50%, where t_{on} denotes the loading time and t_{off} represents the unloading time during a loading cycle. Furthermore, Fig. 9 (c) demonstrates the motion performance of the robot under different voltage parameters. At a duty cycle of 50%, the average velocity of robot decreases as the loading period increases. When t_{on} remains constant, the average velocity also decreases with the increase in unloading time.

5. Conclusion

In this paper, we introduce a flexi-limbed actuator, which uses the dielectrophoretic liquid zipping concept for actuation as a building block for manipulation gripper and soft mobile robots. We establish a theoretical model describing the electromechanical coupling of the flexi-limbed actuator, employing the large deformation theory of the beam and the system energy method. This model is experimentally validated to accurately simulate the actuation behavior of the actuator under voltage excitation. Based on the theoretical model, we investigate the influence of critical design parameters on the actuator's performance. Subsequently, we explore the force response under static voltage and the dynamic response under alternative voltage through experimental methods. Our findings show that the actuator exhibits a blocking force under 7 kV voltage, with a peak response observed at a 9 Hz excitation frequency, which has been captured in an inchworm-like movement.

The flexi-limbed actuator presented here is a novel free-standing structure with straightforward assembly. The innovative use of three flexible electrodes to form a bridge-arch-like configuration ensures strong structural stability and leverages inherent stiffness to rapidly return to its original state when voltage is removed. These features make the actuator well-suited for a range of robotic applications. For example, miniaturized actuators, arranged in series and parallel, can move a soft robot forward or backward, depending on its foot structure, while also enabling steering. The series configuration allows for greater force output, and harmonic actuation pattern, while the parallel arrangement enables more precise control and flexibility. Such arrangements provide adaptable motion for the robot to navigate complex environments. Additionally, with careful implementation of a soft interface layer, this can be adapted for flexible gripping tasks, enabling the manipulation of delicate or irregularly shaped items.

While this paper focuses on the static response of the actuator, future work should explore the dynamic behavior, including the impact of silicone oil flow. This is crucial for optimizing control in robotic applications and flexible manipulators which needs further study to demonstrate adaptable manipulation across a wide range of objects.

Declaration

During the preparation of this work, the authors used ChatGPT for proofreading. After using this tool, the authors reviewed and edited the content as needed and took full responsibility for the content of the publication.

CRediT authorship contribution statement

Wenjie Sun: Writing – review & editing, Methodology, Funding acquisition, Conceptualization. **Yuejun Xu:** Methodology. **Majid Taghavi:** Writing – review & editing, Supervision, Resources.

Declaration of competing interest

The authors declare the following financial interests/personal relationships which may be considered as potential competing interests:

Wenjie Sun reports financial support was provided by China Scholarship Council. Wenjie Sun reports financial support was provided by Natural Science Foundation of Shannxi Province of China. If there are other authors, they declare that they have no known competing financial interests or personal relationships that could have appeared to influence the work reported in this paper.

Acknowledgements

This work was supported by Natural Science Foundation of Shannxi Province of China (No. 2024JC-YBQN-0028) and China Scholarship Council (No. 202108610144). M.T acknowledges Imperial College Bioengineering Fellowship.

Appendix A. The bending strain energy of beam based on CBCM method

According to the CBCM theory, in a multi-beam system, assuming that the j beam is divided into N segments of micro-beams, a local coordinate system $x_i^j o_i^j y_i^j$ is established at the front end of micro-beam i. The load on micro-beam i at the end is represented by P_i^j, F_i^j, and M_i^j (as shown in Fig. 2 (b)), and the displacements and angles of rotation at the end of the micro-beams are denoted as Λ_i^j, Δ_i^j, and α_i^j. Assuming L_j, E_jI_j, and T_j represents the length, bending stiffness, and beam thickness of beam j, respectively, the following dimensionless parameters are defined:

$$p_i^j = \frac{P_i^j L_j^2}{N^2 E_j I_j}, f_i^j = \frac{F_i^j L_j^2}{N^2 E_j I_j}, m_i^j = \frac{M_i^j L_j^2}{N^2 E_j I_j}, \lambda_i^j = \frac{N\Lambda_i^j}{L_j}, \delta_i^j = \frac{N\Delta_i^j}{L_j}, t_j = \frac{NT_j}{L_j} \ . \tag{A.1}$$

In this case, the equilibrium control equation for each microbeam in beam j can be expressed as [70]:

$$\begin{bmatrix} cos\theta_i^j & sin\theta_i^j & 0 \\ -sin\theta_i^j & cos\theta_i^j & 0 \\ \left(1+\lambda_i^j\right) & -\delta_i^j & 1 \end{bmatrix} \begin{bmatrix} f_i^j \\ p_i^j \\ m_i^j \end{bmatrix} = \begin{bmatrix} f_1^j \\ p_1^j \\ m_{i-1}^j \end{bmatrix} ,$$

$$\lambda_i^j = \frac{t_j^2 p_i^j}{12} - \frac{1}{60}\begin{bmatrix} \delta_i^j & \alpha_i^j \end{bmatrix} \begin{bmatrix} 36 & -3 \\ -3 & 4 \end{bmatrix} \begin{bmatrix} \delta_i^j \\ \alpha_i^j \end{bmatrix} - \frac{p_i^j}{6300}\begin{bmatrix} \delta_i^j & \alpha_i^j \end{bmatrix} \begin{bmatrix} -9 & 4.5 \\ 4.5 & -11 \end{bmatrix} \begin{bmatrix} \delta_i^j \\ \alpha_i^j \end{bmatrix} , \tag{A.2}$$

where the force balance relationship between microbeam i and microbeam 1 in beam j is ($i = 2, \cdots, N$):

$$p_1^j = p_o^j = \frac{P_o^j L_j^2}{N^2 E_j I_j}, f_1^j = f_o^j = \frac{F_o^j L_j^2}{N^2 E_j I_j}, m_1^j = m_o^j = \frac{M_o^j L_j^2}{N^2 E_j I_j}, \theta_1^j = 0, \theta_i^j = \sum_{k=1}^{i-1} \alpha_k^j \ . \tag{A.3}$$

The deformation of each microbeam i in beam j can be obtained by solving the 6 N equation in Equation A.2 and Equation A.3. The end displacements X_o^j, Y_o^j, and the angle of rotation θ_o^j of the jth beam in its reference coordinate system, $x_1^j o_1^j y_1^j$, can be determined by the following coordinate transformations:

$$\begin{aligned} X_o^j &= \sum_{i=1}^{N} \frac{L_j}{N}\left[\left(1+\lambda_i^j\right) cos\theta_i^j - \delta_i^j sin\theta_i^j\right] , \\ Y_o^j &= \sum_{i=1}^{N} \frac{L_j}{N}\left[\left(1+\lambda_i^j\right) sin\theta_i^j + \delta_i^j cos\theta_i^j\right] , \\ \theta_o^j &= \sum_{i=1}^{N} \alpha_i^j \end{aligned} \tag{A.4}$$

Therefore, the bending strain energy V^j of beam j can be calculated by the following equation:

$$V^j = \sum_{i=1}^{N} \frac{NE_j I_j}{L_j}\left[\frac{\left(t_j p_i^j\right)^2}{24} + \begin{bmatrix} \delta_i^j & \alpha_i^j \end{bmatrix} \begin{bmatrix} 6 & -3 \\ -3 & 2 \end{bmatrix} \begin{bmatrix} \delta_i^j \\ \alpha_i^j \end{bmatrix} - \frac{\left(p_i^j\right)^2}{12600}\begin{bmatrix} \delta_i^j & \alpha_i^j \end{bmatrix} \begin{bmatrix} -9 & 4.5 \\ 4.5 & -11 \end{bmatrix} \begin{bmatrix} \delta_i^j \\ \alpha_i^j \end{bmatrix}\right] . \tag{A.5}$$

Data availability

Data supporting this study are openly available from Zenodo at [https://doi.org/10.5281/zenodo.13800869].

References

[1] Rus D, Tolley MT. Design, fabrication and control of soft robots. Nature 2015;521:467–75. https://doi.org/10.1038/nature14543.

[2] Laschi C, Mazzolai B, Cianchetti M. Soft robotics: Technologies and systems pushing the boundaries of robot abilities. Sci Robot 2016;1:eaah3690. https://doi.org/10.1126/scirobotics.aah3690.

[3] Rich SI, Wood RJ, Majidi C. Untethered soft robotics. Nat Electron 2018;1:102–12. https://doi.org/10.1038/s41928-018-0024-1.

[4] Pelrine R, Kornbluh R, Pei Q, Joseph J. High-Speed Electrically Actuated Elastomers with Strain Greater Than 100%. Science (1979) 2000;287:836–9. https://doi.org/10.1126/science.287.5454.836.

[5] Acome E, Mitchell SK, Morrissey TG, Emmett MB, Benjamin C, King M, et al. Hydraulically Amplified Self-Healing Electrostatic Actuators with Muscle-Like Performance. Science (1979) 2018;359:61–5. https://doi.org/10.1126/science.aao6139.

[6] Shi Y, Askounis E, Plamthottam R, Libby T, Peng Z, Youssef K, et al. A processable, high-performance dielectric elastomer and multilayering process. Science (1979) 2022;377:228–32. https://doi.org/10.1126/science.abn0099.

[7] Kim Y, Yuk H, Zhao R, Chester SA, Zhao X. Printing ferromagnetic domains for untethered fast-transforming soft materials. Nature 2018;558:274–9. https://doi.org/10.1038/s41586-018-0185-0.

[8] Mao G, Drack M, Karami-Mosammam M, Wirthl D, Stockinger T, Schwödiauer R, et al. Soft electromagnetic actuators. Sci Adv 2020;6:eabc0251. https://doi.org/10.1126/sciadv.abc0251.

[9] Ze Q, Kuang X, Wu S, Wong J, Montgomery SM, Zhang R, et al. Magnetic shape memory polymers with integrated multifunctional shape manipulation. Adv Mater 2020;32:1906657. https://doi.org/10.1002/adma.201906657.

[10] Yuan J, Neri W, Zakri C, Merzeau P, Kratz K, Lendlein A, et al. Shape memory nanocomposite fibers for untethered high-energy microengines. Science (1979) 2019;365:155–8. https://doi.org/10.1126/science.aaw3722.

[11] Miriyev A, Stack K, Lipson H. Soft material for soft actuators. Nat Commun 2017;8:596. https://doi.org/10.1038/s41467-017-00685-3.

[12] He Q, Wang Z, Wang Y, Wang Z, Li C, Annapooranan R, et al. Electrospun liquid crystal elastomer microfiber actuator. Sci Robot 2021;6:eabi9704. https://doi.org/10.1126/scirobotics.abi9704.

[13] Kwan KW, Li SJ, Hau NY, Li W-D, Feng SP, Ngan AHW. Light-stimulated actuators based on nickel hydroxide-oxyhydroxide. Sci Robot 2018;3:eaat4051. https://doi.org/10.1126/scirobotics.aat4051.

[14] Wani OM, Zeng H, Priimagi A. A light-driven artificial flytrap. Nat Commun 2017;8:15546. https://doi.org/10.1038/ncomms15546.

[15] Chen Y, Yang J, Zhang X, Feng Y, Zeng H, Wang L, et al. Light-driven bimorph soft actuators: design, fabrication, and properties. Mater Horiz 2021;8:728–57. https://doi.org/10.1039/D0MH01406K.

[16] Jones TJ, Jambon-Puillet E, Marthelot J, Brun P-T. Bubble casting soft robotics. Nature 2021;599:229–33. https://doi.org/10.1038/s41586-021-04029-6.

[17] Preston DJ, Jiang HJ, Sanchez V, Rothemund P, Rawson J, Nemitz MP, et al. A soft ring oscillator. Sci Robot 2019;4:eaaw5496. https://doi.org/10.1126/scirobotics.aaw5496.

[18] Morin SA, Shepherd RF, Kwok SW, Stokes AA, Nemiroski A, Whitesides GM. Camouflage and display for soft machines. Science (1979) 2012;337:828–32. https://doi.org/10.1126/science.1222149.

[19] Wehner M, Truby RL, Fitzgerald DJ, Mosadegh B, Whitesides GM, Lewis JA, et al. An integrated design and fabrication strategy for entirely soft, autonomous robots. Nature 2016;536:451–5. https://doi.org/10.1038/nature19100.

[20] Bartlett NW, Tolley MT, Overvelde JTB, Weaver JC, Mosadegh B, Bertoldi K, et al. A 3D-printed, functionally graded soft robot powered by combustion. Science (1979) 2015;349:161–5. https://doi.org/10.1126/science.aab0129.

[21] Fusi G, Del Giudice D, Skarsetz O, Di Stefano S, Walther A. Autonomous soft robots empowered by chemical reaction networks. Adv Mater 2023;35:2209870. https://doi.org/10.1002/adma.202209870.

[22] El-Atab N, Mishra RB, Al-Modaf F, Joharji L, Alsharif AA, Alamoudi H, et al. Soft actuators for soft robotic applications: a review. Adv Intell Syst 2020;2:2000128. https://doi.org/10.1002/aisy.202000128.

[23] Li M, Pal A, Aghakhani A, Pena-Francesch A, Sitti M. Soft actuators for real-world applications. Nat Rev Mater 2022;7:235–49. https://doi.org/10.1038/s41578-021-00389-7.

[24] Ahn J, Gu J, Choi J, Han C, Jeong Y, Park J, et al. A review of recent advances in electrically driven polymer-based flexible actuators: smart materials, structures, and their applications. Adv Mater Technol 2022;7:2200041. https://doi.org/10.1002/admt.202200041.

[25] Lu T, Ma C, Wang T. Mechanics of dielectric elastomer structures: a review. Extreme Mech Lett 2020;38:100752. https://doi.org/10.1016/j.eml.2020.100752.

[26] O'Halloran A, O'Malley F, McHugh P. A review on dielectric elastomer actuators, technology, applications, and challenges. J Appl Phys 2008;104:071101. https://doi.org/10.1063/1.2981642.

[27] Guo Y, Liu L, Liu Y, Leng J. Review of dielectric elastomer actuators and their applications in soft robots. Adv Intell Syst 2021;3:2000282. https://doi.org/10.1002/aisy.202000282.

[28] Li G, Wong T-W, Shih B, Guo C, Wang L, Liu J, et al. Bioinspired soft robots for deep-sea exploration. Nat Commun 2023;14:7097. https://doi.org/10.1038/s41467-023-42882-3.

[29] Li G, Chen X, Zhou F, Liang Y, Xiao Y, Cao X, et al. Self-powered soft robot in the Mariana Trench. Nature 2021;591:66–71. https://doi.org/10.1038/s41586-020-03153-z.

[30] Christianson C, Goldberg NN, Deheyn DD, Cai S, Tolley MT. Translucent soft robots driven by frameless fluid electrode dielectric elastomer actuators. Sci Robot 2018;3:eaat1893. https://doi.org/10.1126/scirobotics.aat1893.

[31] Chen Y, Zhao H, Mao J, Chirarattananon P, Helbling EF, Hyun NP, et al. Controlled flight of a microrobot powered by soft artificial muscles. Nature 2019;575:324–9. https://doi.org/10.1038/s41586-019-1737-7.

[32] Ren Z, Kim S, Ji X, Zhu W, Niroui F, Kong J, et al. A high-lift micro-aerial-robot powered by low-voltage and long-endurance dielectric elastomer actuators. Adv Mater 2022;34:2106757. https://doi.org/10.1002/adma.202106757.

[33] Kim S, Hsiao Y-H, Lee Y, Zhu W, Ren Z, Niroui F, et al. Laser-assisted failure recovery for dielectric elastomer actuators in aerial robots. Sci Robot 2023;8:eadf4278. https://doi.org/10.1126/scirobotics.adf4278.

[34] Gu G, Zou J, Zhao R, Zhao X, Zhu X. Soft wall-climbing robots. Sci Robot 2018.

[35] Tang C, Du B, Jiang S, Shao Q, Dong X, Liu X-J, et al. A pipeline inspection robot for navigating tubular environments in the sub-centimeter scale. Sci Robot 2022;7:eabm8597. https://doi.org/10.1126/scirobotics.abm8597.

[36] Sun W, Li B, Zhang F, Fang C, Lu Y, Gao X, et al. TENG-Bot: Triboelectric nanogenerator powered soft robot made of uni-directional dielectric elastomer. Nano Energy 2021;85:106012. https://doi.org/10.1016/j.nanoen.2021.106012.

[37] Pu J, Meng Y, Xie Z, Peng Z, Wu J, Shi Y, et al. A unimorph nanocomposite dielectric elastomer for large out-of-plane actuation. Sci Adv 2022;8:eabm6200. https://doi.org/10.1126/sciadv.abm6200.

[38] Chen B, Sun W, Lu J, Yang J, Chen Y, Zhou J, et al. All-solid ionic eye. J Appl Mech 2020;88. https://doi.org/10.1115/1.4049198.

[39] She A, Zhang S, Shian S, Clarke DR, Capasso F. Adaptive metalenses with simultaneous electrical control of focal length, astigmatism, and shift. Sci Adv 2018;4:eaap9957. https://doi.org/10.1126/sciadv.aap9957.

[40] Xu Z, Bao K, Di K, Chen H, Tan J, Xie X, et al. High-performance dielectric elastomer nanogenerator for efficient energy harvesting and sensing via alternative current method. Adv Sci 2022;9:2201098. https://doi.org/10.1002/advs.202201098.

[41] Jiang Y, Liu S, Zhong M, Zhang L, Ning N, Tian M. Optimizing energy harvesting performance of cone dielectric elastomer generator based on VHB elastomer. Nano Energy 2020;71:104606. https://doi.org/10.1016/j.nanoen.2020.104606.

[42] Moretti G, Papini GPR, Righi M, Forehand D, Ingram D, Vertechy R, et al. Resonant wave energy harvester based on dielectric elastomer generator. Smart Mater Struct 2018;27:035015. https://doi.org/10.1088/1361-665X/aaab1e.

[43] Poulin A, Saygili Demir C, Rosset S, Petrova TV, Shea H. Dielectric elastomer actuator for mechanical loading of 2D cell cultures. Lab Chip 2016;16:3788–94. https://doi.org/10.1039/C6LC00903D.

[44] Gao C, Li Z, Zou J, Cheng J, Jiang K, Liu C, et al. Mechanical effect on gene transfection based on dielectric elastomer actuator. ACS Appl Bio Mater 2020;3:2617–25. https://doi.org/10.1021/acsabm.9b01199.

[45] Huang J, Shian S, Diebold RM, Suo Z, Clarke DR. The thickness and stretch dependence of the electrical breakdown strength of an acrylic dielectric elastomer. Appl Phys Lett 2012;101:122905. https://doi.org/10.1063/1.4754549.

[46] Kofod G. The static actuation of dielectric elastomer actuators: how does pre-stretch improve actuation? J Phys D: Appl Phys 2008;41:215405. https://doi.org/10.1088/0022-3727/41/21/215405.

[47] Plante J-S, Dubowsky S. Large-scale failure modes of dielectric elastomer actuators. Int J Solids Struct 2006;43:7727–51. https://doi.org/10.1016/j.ijsolstr.2006.03.026.

[48] Gu G-Y, Gupta U, Zhu J, Zhu L-M, Zhu X. Modeling of viscoelastic electromechanical behavior in a soft dielectric elastomer actuator. IEEE Trans Robot 2017;33:1263–71. https://doi.org/10.1109/TRO.2017.2706285.

[49] Rothemund P, Kellaris N, Mitchell SK, Acome E, Keplinger C. HASEL artificial muscles for a new generation of lifelike robots—recent progress and future opportunities. Adv Mater 2021;33:2003375. https://doi.org/10.1002/adma.202003375.

[50] Kellaris N, Gopaluni Venkata V, Smith GM, Mitchell SK, Keplinger C. Peano-HASEL actuators: muscle-mimetic, electrohydraulic transducers that linearly contract on activation. Sci Robot 2018;3:eaar3276. https://doi.org/10.1126/scirobotics.aar3276.

[51] Rumley EH, Preninger D, Shagan Shomron A, Rothemund P, Hartmann F, Baumgartner M, et al. Biodegradable electrohydraulic actuators for sustainable soft robots. Sci Adv 2023;9:eadf5551. https://doi.org/10.1126/sciadv.adf5551.

[52] Mitchell SK, Wang X, Acome E, Martin T, Ly K, Kellaris N, et al. An easy-to-implement toolkit to create versatile and high-performance HASEL actuators for untethered soft robots. Adv Sci 2019;6:1900178. https://doi.org/10.1002/advs.201900178.

[53] Kellaris N, Rothemund P, Zeng Y, Mitchell SK, Smith GM, Jayaram K, et al. Spider-inspired electrohydraulic actuators for fast, soft-actuated joints. Adv Sci 2021;8:2100916. https://doi.org/10.1002/advs.202100916.

[54] Pirozzi I, Kight A, Liang X, Han AK, Ennis DB, Hiesinger W, et al. Electrohydraulic vascular compression device (e-VaC) with integrated sensing and controls. Adv Mater Technol 2023;8:2201196. https://doi.org/10.1002/admt.202201196.

[55] Chen R, Yuan Z, Guo J, Bai L, Zhu X, Liu F, et al. Legless soft robots capable of rapid, continuous, and steered jumping. Nat Commun 2021;12:7028. https://doi.org/10.1038/s41467-021-27265-w.

[56] Wang X, Mitchell SK, Rumley EH, Rothemund P, Keplinger C. High-strain Peano-HASEL actuators. Adv Funct Mater 2020;30:1908821. https://doi.org/10.1002/adfm.201908821.

[57] Taghavi M, Helps T, Rossiter J. Electro-ribbon actuators and electro-origami robots. Sci Robot 2018;3:eaau9795. https://doi.org/10.1126/scirobotics.aau9795.

[58] Helps T, Romero C, Taghavi M, Conn AT, Rossiter J. Liquid-amplified zipping actuators for micro-air vehicles with transmission-free flapping. Sci Robot 2022;7:eabi8189. https://doi.org/10.1126/scirobotics.abi8189.

[59] Diteesawat RS, Helps T, Taghavi M, Rossiter J. Electro-pneumatic pumps for soft robotics. Sci Robot 2021;6:eabc3721. https://doi.org/10.1126/scirobotics.abc3721.

[60] Fraai T, Wen J, Taghavi M. Electrically zipping bending actuators for prosthetic fingers. IEEE Robot Autom Lett 2023;8:7472–8. https://doi.org/10.1109/LRA.2023.3317676.

[61] Hou N, Wen J, Pan Y, Taghavi M. Origami-inspired modular electro-ribbon actuator for multi-degrees of freedom motion. Adv Intell Syst n.d.;n/a:2300738. https://doi.org/10.1002/aisy.202300738.

[62] Garrad M, Zadeh MN, Romero C, Scarpa F, Conn AT, Rossiter J. Design and characterisation of a muscle-mimetic dielectrophoretic ratcheting actuator. IEEE Robot Autom Lett 2022;7:3938–44. https://doi.org/10.1109/LRA.2022.3149039.

[63] Xu Y, Burdet E, Taghavi M. Electromechanical model for electro-ribbon actuators. Int J Mech Sci 2024;275:109340. https://doi.org/10.1016/j.ijmecsci.2024.109340.

[64] Castro B, Diteesawat RS, Taghavi M, Rossiter J. Modular simulation framework for Electro-ribbon Actuators. In: 2021 IEEE 4th International Conference on Soft Robotics (RoboSoft); 2021. p. 215–21. https://doi.org/10.1109/RoboSoft51838.2021.9479259.

[65] Cao X, Zou W, Zhuo J, Ruan D, Xu Y, Zhou F, et al. Design and modeling of an electro-hydraulic buoyancy adjustment actuator. AIP Adv 2023;13:105115. https://doi.org/10.1063/5.0149812.

[66] Kellaris N, Venkata VG, Rothemund P, Keplinger C. An analytical model for the design of Peano-HASEL actuators with drastically improved performance. Extreme Mech Lett 2019;29:100449. https://doi.org/10.1016/j.eml.2019.100449.

[67] Rosset S, Araromi OA, Shintake J, Shea HR. Model and design of dielectric elastomer minimum energy structures. Smart Mater Struct 2014;23:085021. https://doi.org/10.1088/0964-1726/23/8/085021.

[68] Chen G, Ma F, Hao G, Zhu W. Modeling large deflections of initially curved beams in compliant mechanisms using chained beam constraint model. J Mech Robot 2019;11:011002. https://doi.org/10.1115/1.4041585.

[69] Ma F, Chen G. Kinetostatic modeling and characterization of compliant mechanisms containing flexible beams of variable effective length. Mech Mach Theory 2020;147:103770. https://doi.org/10.1016/j.mechmachtheory.2019.103770.

[70] Ma F, Chen G. Modeling Large Planar Deflections of Flexible Beams in Compliant Mechanisms Using Chained Beam-Constraint-Model1. J Mech Robot 2016;8:021018. https://doi.org/10.1115/1.4031028.

[71] Kim H, Ma J, Kim M, Nam J, Kyung K-U. High-output force electrohydraulic actuator powered by induced interfacial charges. Adv Intell Syst 2021;3:2100006. https://doi.org/10.1002/aisy.202100006.

[72] Sun W, Liang H, Zhang F, Wang H, Lu Y, Li B, et al. Dielectric elastomer minimum energy structure with a unidirectional actuation for a soft crawling robot: Design, modeling, and kinematic study. Int J Mech Sci 2023;238:107837. https://doi.org/10.1016/j.ijmecsci.2022.107837.

[73] Kim S, Cha Y. A soft crawling robot with a modular design based on electrohydraulic actuator. iScience 2023;26:106726. https://doi.org/10.1016/j.isci.2023.106726.

[74] Du B, Tang C, Jiang S, Wang Y, Liu X-J, Zhao H. High-speed rotary motor for multidomain operations driven by resonant dielectric elastomer actuators. Adv Intell Syst 2023;5:2300243. https://doi.org/10.1002/aisy.202300243.

[75] Gao X, Cao C, Guo J, Conn A. Elastic electroadhesion with rapid release by integrated resonant vibration. Adv Mater Technol 2019;4:1800378. https://doi.org/10.1002/admt.201800378.

[76] Tang C, Li B, Fang H, Li Z, Chen H. A speedy, amphibian, robotic cube: resonance actuation by a dielectric elastomer. Sensors Actuators A 2018;270:1–7. https://doi.org/10.1016/j.sna.2017.12.003.

[77] Yang D, Mosadegh B, Ainla A, Lee B, Khashai F, Suo Z, et al. Buckling of elastomeric beams enables actuation of soft machines. Adv Mater 2015;27:6323–7. https://doi.org/10.1002/adma.201503188.
[78] Zhang Y, Yang D, Yan P, Zhou P, Zou J, Gu G. Inchworm inspired multimodal soft robots with crawling, climbing, and transitioning locomotion. IEEE Trans Robot 2022;38:1806–19. https://doi.org/10.1109/TRO.2021.3115257.
[79] Hu T, Lu X, Liu J. Inchworm-like soft robot with multimodal locomotion using an acrylic stick-constrained dielectric elastomer actuator. Adv Intell Syst 2023;5: 2200209. https://doi.org/10.1002/aisy.202200209.
[80] Sun W, Liu F, Ma Z, Li C, Zhou J. Soft mobile robots driven by foldable dielectric elastomer actuators. J Appl Phys 2016;120:084901. https://doi.org/10.1063/1.4960718.
[81] Li T, Zou Z, Mao G, Yang X, Liang Y, Li C, et al. Agile and resilient insect-scale robot. Soft Robot 2019;6:133–41. https://doi.org/10.1089/soro.2018.0053.